Editors' Suggestion

Segmented flows of viscous threads in microchannels

Thomas Cubaud*

Department of Mechanical Engineering, Stony Brook University, Stony Brook, New York 11794, USA

(Received 17 April 2019; published 8 August 2019)

The passage of microfluidic droplets in miscible thread-forming flows is shown to improve the mixing efficiency of low- and high-viscosity fluids at the small scale. Hydrodynamic interactions between recirculating flow patterns and viscous core-annular flows are experimentally investigated in square microchannels. The deformation of thick segmented flows injected in thin fluids is examined through the evolution of droplet size, spacing, and velocity along a square microchannel. Droplets also help in probing the various states of lubrication of the viscous central stream in the bulging, tubing, and threading regimes at various capillary and Péclet numbers. A range of intriguing flow phenomena is revealed using a dual approach based on thread and droplet mutual behaviors, including droplet breakup, formation of low-viscosity currents, thread splitting, viscous fingering, and viscous buckling instabilities. The thread-forming ability of miscible fluids having large viscosity contrasts is discussed in conjunction with mixing applications where a thinner or a viscosifier is continuously added to a viscosity-differing fluid in confined microsystems.

DOI: 10.1103/PhysRevFluids.4.084201

I. INTRODUCTION

The interaction and combination of fluid streams has long attracted scientific and technological interest. In the case of liquids, fluid properties result from their molecular nature and strongly influence motion [1] and multiphase flow configuration [2,3]. While dynamic viscosity correlates with molecular weight, interfacial properties are contingent on molecular affinity and liquid pairs made of molecules having similar polarities are typically miscible and mix due to diffusion. By contrast, liquids having disparate molecular polarities are generally immiscible and display interfacial tension favoring droplet formation during dispersion. These basic fluid properties are of considerable significance in microfluidic systems where the composition of droplets can be finely controlled to form microreactors for biomedical and material synthesis applications [4–6]. In microchannels, interfacial tension finds use to encapsulate complex materials [7] and compartment miscible fluids into segmented flows [8]. Such flows are known to enhance mixing due to the formation of recirculating flow patterns between moving fluid partitions. As a result, droplet- or bubble-based microfluidic methods have been implemented to homogenize the composition of fluids having similar viscosities [9]. Relatively less is known, however, about the use of segmented flows to continuously enhance mixing of fluids having large variations in viscosity [10,11].

The problem of in-line mixing of thin and thick fluids is rather complex due to the evolution of the local viscosity as fluids blend along a fluidic system. Depending on the type of applications, one may want to rapidly increase the viscosity of a thin fluid, such as adding a viscosifier to a drilling fluid, or to reduce the viscosity of a thick material, for instance, by adding a thinner to a petroleum product. At the small scale, various methods have been developed to circumvent the

*thomas.cubaud@stonybrook.edu

limitation associated with mixing highly viscous fluids [12], such as interconnected multichannel network [13], combination of pneumatic valves and recirculation loops [14], or acoustically induced bubbles [15,16]. In the presence of large viscosity contrasts, however, fluids can also self-lubricate and the more viscous phase forms slender threads convected in the low-viscosity fluid [17]. Previous work has shown that microfluidic threads are subject to numerous hydrodynamic destabilization processes, such as diffusive and inertial instabilities [18], as well as viscous buckling instabilities [19–22], which enable manipulations of fluid interfacial area to reduce the diffusional path and enhance mixing. Better understanding of flow interaction between lubricated threads and droplets is therefore promising for the development of passive techniques to address the challenging problem of continuously mixing widely disparate fluids at the small scale.

Here, the thread-forming ability of viscous fluids is experimentally investigated in the presence of segmented flows of droplets in the high-viscosity stream. A complementary approach is adopted where the thread size is systematically varied for low, medium, and large concentrations of droplets. Examining the mutual relationships between droplet motion and thread formation helps reveal a variety of basic fluid structures and intriguing flow phenomena. This study begins with focus on droplet dynamics during the injection of segmented flows into thread-forming stratifications. The evolution of droplet velocity, size, and spacing is characterized at various capillary numbers and modifications of aspect ratio and wavelength of segmented flows are discussed. The second part centers on the continuous phase and examines alteration of thread flow regimes due to the presence of relatively slow moving droplets. Such droplets enable probing the structure of viscous lubricated flows and induces flow phenomena, such as low-viscosity fluid bulging, viscous fingering, thread thinning, and viscous buckling instabilities. The duality in the evolution of droplet and thread is used to learn from one another. As segmented flows of viscous threads are inherently unstable due to velocity differences between core-annular and droplet flows, regions of improved mixing efficiency are delineated in the droplet-thread parameter space.

II. EXPERIMENTAL METHODS

Microfluidic segmented flows of droplets are continuously generated to produce regular flow patterns that are injected into the central stream of a viscous thread further downstream. A schematic of the microfluidic method employed is shown in Fig. 1(a). Microchannels are made of etched-through silicon wafers that are anodically bonded between two borosilicate glass plates. Microchips are placed on top of an inverted microscope equipped with a high-speed camera and fluids are continuously injected into the microfluidic platform using high-pressure syringe pumps. Microchannels are square in cross section and have a height of $h = 250\,\mu$m. Liquid $L1$ is made of de-ionized (DI) water of viscosity $\eta_1 = 1$ cP and is injected in the central channel of the first square focusing section at flow rate Q_1. The liquid $L2$, a high-viscosity silicone of viscosity $\eta_2 = 486$ cP, is symmetrically inserted from the side channels at a total flow rate Q_2.

Initial flow patterns consist of droplets having a size d_0 separated by a distance L_0. Segmented flows comprise of a repetition of flow cells of length $\lambda_0 = d_0 + L_0$ and period $T_0 = \lambda_0/V_0$, where the droplet velocity $V_0 = k_0(Q_1 + Q_2)/h^2$. The mobility coefficient k_0 is on the order of unity and has a weak dependence on droplet size d_0 and capillary number $\mathrm{Ca}_0 = \eta_2 V_0/\gamma_{12}$, where γ_{12} is the interfacial tension between $L1$ and $L2$ [23,24]. Tuning the injection flow rates Q_1 and Q_2 allows for the emergence of a variety of flow patterns from concentrated droplet flows with large d_0 and small L_0 to diluted droplet regimes with small d_0 and large L_0. Using this technique, a variety of segmented microflows are generated and continuously injected through the central channel of a second focusing section where $L3$, a low-viscosity silicone oil of viscosity $\eta_3 = 4.59$ or 0.49 cP, is injected from the side channels at a total flow rate Q_3. The interfacial tension between DI water and the different silicone oils is nearly constant, $\gamma_{12} \approx 35$mN/m, which permits exploring the influence of moderate and large viscosity contrasts $\chi = \eta_2/\eta_3 = 106$ and 982 between miscible fluids. Since the low-viscosity silicone oil $L3$ having $\eta_3 = 0.49\,cP$ is strongly diffusive, the $L2/L3$ fluid pair is labeled "$D3$" and has a low Schmidt number, $Sc = \eta_2/(\rho_2 D) = 1.2 \times 10^3$, where D is the $L2/L3$

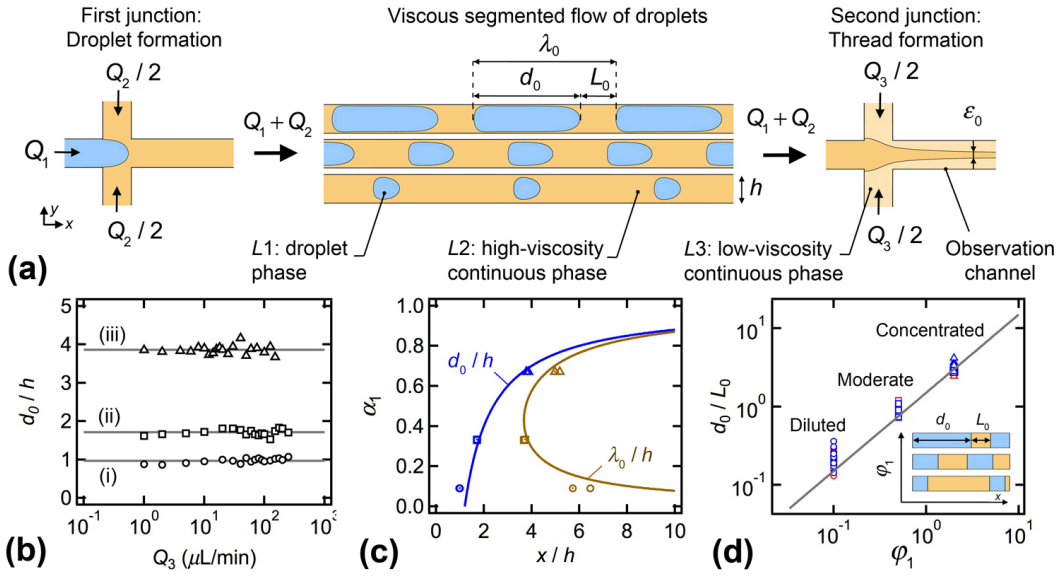

FIG. 1. (a) Schematics of injection scheme with two-step hydrodynamic focusing section in square microchannels. (b) Initial droplet size d_0/h as a function of downstream flow rate Q_3 for various initial droplet regimes, fluid group $M2$, flow rates in μl/min: (i) diluted, $d_0/h \approx 0.97$, and $(Q_1, Q_2) = (5, 50)$ with $\mathrm{Ca}_0 \approx 0.38$; (ii) moderate, $d_0/h \approx 1.71$, and (25, 50) with $\mathrm{Ca}_0 \sim 0.48$; and (iii) concentrated, $d_0/h \approx 3.86$, and (20, 10) with $\mathrm{Ca}_0 \approx 0.19$. (c) Initial flow morphologies with spatial extent of average initial droplet size d_0/h and wavelength λ_0 at various initial droplet fraction α_1. Solid lines: see main text. (d) Evolution of initial d_0/L_0 as a function of φ_1 for both fluid pairs. Solid line: $d_0/L_0 = 1.5\varphi_0$. Inset: linear representation of initial segmented flows.

diffusion coefficient, which is estimated as $D = 5.6 \times 10^{-10}\ \mathrm{m}^2/\mathrm{s}$ similar to previous work [18]. In the case where the oil $L3$ has a viscosity $\eta_3 = 4.59$, the fluid pair $L2/L3$ is referred to as "$M2$" and has a large $Sc = 8 \times 10^4$ given the relatively low intermolecular diffusivity $D = 6.0 \times 10^{-11}\ \mathrm{m}^2/\mathrm{s}$ between these fluids. Using the pair $D3$ grants access to diffusive miscible flow regimes, while the pair $M2$ is associated with weakly diffusive thread regimes. When advection is present, flow regimes are typically classified based on Péclet number $\mathrm{Pe} = hV/D$.

The flow configuration where the more viscous fluid is unsheathed with a less viscous liquid permits the formation of lubricated threads that are prone to a variety of hydrodynamic instabilities [18]. In this work, droplets are shown to significantly disrupt self-lubricating viscous layers in the observation channel downstream of the second junction. To proceed methodically, the role of the initial segmented flow morphology on threads is examined using three droplet concentrations $\alpha_1 = Q_1/(Q_1 + Q_2)$, including $\alpha_1 = 0.09$, 0.33, and 0.67 for the diluted, moderate, and concentrated regimes, respectively Fig. 1(a). In a typical series of experiments, Q_1 and Q_2 are fixed and the low-viscosity flow rate Q_3 is increased according to a logarithmic scale in the second section to document a large range of operating conditions. The influence of the initial capillary number $\mathrm{Ca}_0 = \eta_2 V_0/\gamma_{12}$ is also tested with variations of Q_1 and Q_2 for fixed α_1. To probe the role of the three droplet concentrations α_1, focus is given on experiments conducted at large initial capillary number $\mathrm{Ca}_0 \sim 0.4$.

The camera field of view includes both the second focusing section to measure initial droplet size d_0, spacing L_0, and velocity V_0, and the observation channel to quantitatively examine the reciprocal interaction between microfluidic droplets and threads. To ensure consistency in initial conditions, the droplet size d_0 is measured upstream from the second junction at large initial Ca_0 and data show that, for fixed α_1, monodisperse droplets of constant d_0 are produced independently of downstream flow conditions for variations in Q_3 over two orders of magnitude [Fig. 1(b)]. While injecting

$L3$ significantly modifies downstream pressure, measurements suggest that, for flow rate-driven systems with nondeformable walls, the droplet size d_0 does not depend on downstream absolute pressure conditions but rather on the magnitude of Q_1 and Q_2, which controls the relative pressure drop in the first junction. This property renders possible the systematic study of the influence of droplet size on thread-forming flows.

The formation of low-viscosity droplets in a viscous continuous phase in hydrodynamic focusing sections is related to the generation of bubbles [25] where the internal viscosity is negligible compared to that of the external phase. In this situation, a simple argument for the droplet size corresponds to $d_0 \sim V_0 T_B$ where the time T_B scales with the filling of the junction by the external fluid $T_B \sim h^3/Q_2$, which yields good agreement with the data as $d_0/h = k_0/(1-\alpha_1)$ with $k_0 = 1.2$ [Fig. 1(c)]. Once the droplet size d_0 is known, the spacing L_0 can be deduced from a linear mass conservation argument within a unit cell of the segmented flow over T_0 according to $d_0 h^2 \sim Q_1 T_0$ and $L_0 h^2 \sim Q_2 T_0$, which yields $d_0/L_0 \sim \varphi_1$ where the initial droplet flow rate ratio is $\varphi_1 = Q_1/Q_2$. Therefore, the wavelength $\lambda_0 = d_0 + L_0$ is expected to scale as $\lambda_0/h \sim k_0/[\alpha_1(1-\alpha_1)]$. For the three droplet concentrations α_1 at large Ca_0, data for λ_0 show good agreement with previous relationships for both fluids $D3$ and $M2$ when the spherical cap of droplets is taken into account such as $(d_0/h - \pi/6)/(L_0/h + \pi/6) \sim \varphi_1$ [Fig. 1(c)]. Overall, beside relatively small variations in the droplet shape, the quantity d_0/L_0 provides a useful metric for quantifying the linear aspect ratio of segmented flows and the scaling $d_0/L_0 \sim \varphi_1$ is robust for all initial flow conditions investigated in this study [Fig. 1(d)]. In the following, this reproducible system is employed to generate complex microfluidic flow patterns, the morphology of which is analyzed based on the spatial evolution of $\lambda = d + L$ and d/L in the observation channel at various Ca and Pe.

III. FLOW MAPS

The interaction between segmented flows and self-lubricating stratifications at the second junction produces a rich collection of time-dependent flow morphologies. To classify complex flow regimes, a dual approach based on both droplet and thread sizes is implemented. On the one hand, viscous stratifications of the continuous phase significantly alter droplet flows and, on the other hand, the presence of droplets profoundly disrupts thread formation.

From the droplet point of view, the most striking transformation consists in the breaking of large droplets into smaller ones at the junction [Fig. 2(a)]. For a given fluid group, the breaking process depends on the droplet initial size d_0 and fluid injection velocities. When Q_1 and Q_2 are fixed, large droplets break above a critical Q_3. Previous work in a different type of stratum [10] has shown the possibility to nondimensionalize Q_3 by defining a modified capillary number $\mathrm{Ca_M} = \alpha_3 \mathrm{Ca}_3 \chi^{1/2}$ where the influence of relative flow velocities is captured with the added continuous phase fraction $\alpha_3 = Q_3/(Q_1 + Q_2 + Q_3)$, the effect of absolute flow velocity is based on the side injections' capillary number $\mathrm{Ca}_3 = \eta_3 Q_3/(\gamma_{12} h^2)$, and the role of fluid properties is accounted for with the viscosity contrast $\chi = \eta_2/\eta_3$. In this study, break and nonbreakup regimes are well delineated with the relationship $d_0/h = 0.33\,\mathrm{Ca_M}^{-0.3}$ for all parameters investigated. While droplet breakup in microfluidic cross flows has intrinsic fundamental and practical interest, emphasis is given to the nonbreakup regime.

From the thread point of view, droplets act as agitators and help reveal high-viscosity flow structures. In the absence of droplets, when a highly viscous continuous phase is injected from the central channel of a focusing section at Q_A and a low-viscosity fluid is symmetrically inserted from the side channels at Q_B, the thread size is controlled by the flow rate ratio Q_A/Q_B [18]. Here, assuming the segmented flow can be treated as a homogeneous liquid, the thread size is expected to depend on $\varphi_T = (Q_1 + Q_2)/Q_3$. After careful examination of time-evolving flow patterns, it is found that the flow regime observed downstream of the droplet—which is indicated with an arrow in Fig. 2(b)—is a good indicator of flow regimes, which are labeled as bulging, tubing, and threading from large to small φ_T. These regimes are associated with the various degrees of lubrication of the central viscous structure. For large φ_T in the bulging regime, the central structure is in contact with

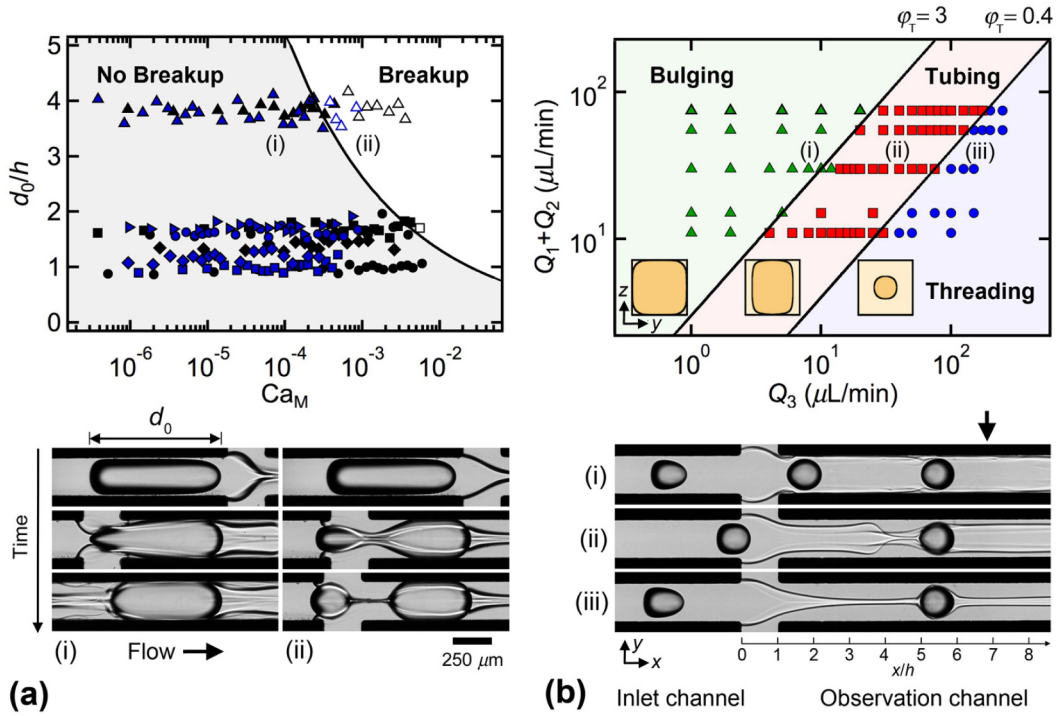

FIG. 2. Droplet- and thread-based phase diagrams. (a) Top: Droplet-based flow map showing breakup and nonbreakup regimes classified as a function of initial droplet size d/h and modified capillary number $\mathrm{Ca_M}$. $\alpha_1 = 0.09$(◯), 0.33 (□), 0.67 (△), groups $D3$ (blue) and $M2$ (black), droplet breakup (open symbol), and nonbreakup (closed symbols). Solid line: $d_0/h = 0.33\mathrm{Ca_M^{-0.3}}$. Bottom: Micrographs of droplet regimes for group $M3$. (b) Top: Flow map based on thread with inner $Q_1 + Q_2$ and outer Q_3 with bulging (△), tubing (□), and threading (◯) regimes, group $M2$. Solid line $\varphi_T = 3$ (bulging-tubing) and $\varphi_T = 0.48$ (tubing-threading). Inset: Schematic of thread cross section downstream of a droplet. Bottom: Micrograph of thread regimes labeled on top map for $\alpha_1 = 0.09$. The arrow indicates location where regimes are determined.

the four walls of the microchannel and the less viscous fluid flows in the gutters. For moderate φ_T in the tubing regime, the thread is lubricated from the side walls but still in contact with the top and bottom walls, while for small φ_T, the central structure of $L2$ is completely lubricated by $L3$ [Fig. 2(b)]. The transition between threading and tubing is found as $\varphi_T = 0.48$ in excellent agreement with previous correlations $\varphi_{\mathrm{Tub}} = 2\chi^{-0.3}$ [18] and the bulging-tubing transition is found at $\varphi_T = 3$ for the fluid group $M2$. The following discussion centers on the nonbreakup droplet regime to probe the role of segmented flows on miscible thread-forming stratifications.

IV. DISTORTED FLOWS OF DROPLETS

The various states of thread lubrication in the observation channel produce distinctive droplet dynamics. The deformation of segmented flows is examined through the evolution of droplet velocity V_D, size d, and spacing L along the microchannel. Control parameters include the initial droplet concentrations $\alpha_1 = Q_1/(Q_1 + Q_2)$ and the thread flow rate ratio $\varphi_{\mathrm{T}} = (Q_1 + Q_2)/Q_3$. In Fig. 3(a), the spatial evolution of the normalized droplet front velocity V_{D}/V_0 is displayed for the three generic droplet concentrations (i) $\alpha_1 = 0.09$, (ii) 0.33, and (iii) 0.67 at large Ca_0. As droplets reduce their speed at the junction between $x/h = 0$ and 1, specific features of each regime further downstream include an overall reduction of V_D in the bulging regime, a progressive rise in the tubing

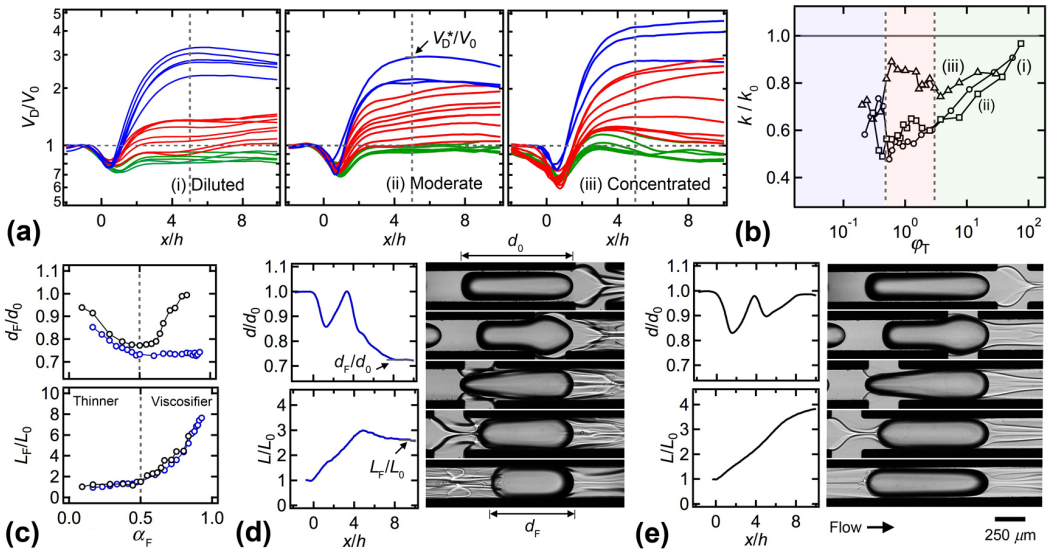

FIG. 3. Evolution of segmented flow dynamics. (a) Spatial distribution of normalized droplet velocities V_D/V_0 for (i) diluted $\alpha_1 = 0.09$, (ii) moderate $\alpha_1 = 0.33$, and (iii) concentrated $\alpha_1 = 0.67$ droplet flows for the weakly diffusive fluid. Colors correspond to thread regimes based on φ_T as Q_3 is varied for fixed Q_1 and Q_2. (b) Relative mobility coefficient k/k_0 as a function of φ_T for various concentrations α_1. (c) Measurements of final normalized length d_F/d_0 and spacing L_F/L_0 of droplets for fixed $Q_1 = 20$ and $Q_2 = 10\,\mu$l/min versus fluid-mixing fraction $\alpha_F = Q_3/(Q_2 + Q_3)$. (d),(e) Evolution of droplet size and spacing in the concentrated regime with micrographs of evolving droplet from $x/h \sim 0$ to 8 (top to bottom), $(Q_1, Q_2, Q_3) = (20, 10, 30)\mu$l/min for fluid group (d) $D3$, and (e) $M2$.

regime, and the presence of a maximum value for low α_1 in the threading regime. These transient droplet behaviors primarily occur due to a localized decrease of the capillary number Ca resulting from the injection of the high-viscosity continuous phase $L2$ in low-viscosity fluid $L3$.

A characteristic droplet velocity V_D^* is measured at $x/h = 5$ and used for the calculation of droplet mobility coefficient k in thread-forming flows defined as $V_D^* = k(Q_1 + Q_2 + Q_3)/h^2$. The initial mobility coefficient k_0 is defined as $V_0 = k_0(Q_1 + Q_2)/h^2$ and provides a reference for comparing droplet velocities based on volumetric flow rates between inlet and observation channel. To refine the understanding of the influence of viscous stratifications on droplet velocity, the relative mobility coefficient k/k_0 is shown as a function of the thread flow rate ratio φ_T for various α_1 in Fig. 3(b). The relative mobility is significantly lower than unity and decreases with Q_3 as more thin fluid is added to the external phase. A sharp gain in mobility is observed at the full lubrication transition between the tubing and the threading regimes for low α_1. In general, the nonmonotonic variations of k/k_0 suggest complex interactions between droplets and the various degrees of central stream lubrication, which requires further examination of droplet dynamics.

As the less viscous fluid $L3$ is injected at the second junction, droplets adapt to their less viscous environment and reduce their length d and grow in width w since the lubricating film thickness $\delta = (h - w)/2$ between droplets and walls decreases for lower Ca. Such phenomenon is illustrated in Fig. 3(c) where the final droplet size d_F and length L_F are measured near the end of the observation channel at $x/h \approx 10$ for both fluid groups $D3$ and $M2$ in the concentrated regime $\alpha_1 = 0.67$ at large Ca_0. The fluid-mixing fraction $\alpha_F = Q_3/(Q_2 + Q_3)$ provides a measure of the relative proportion of thin and thick fluids in the continuous phase and the situation where $\alpha_F < 1/2$ corresponds to the case where a thin fluid is added to a predominantly viscous phase, i.e., in the thinner-mixing situation. By contrast when $\alpha_F < 1/2$, a highly viscous fluid is combined with a large quantity of thin fluid, i.e., in the viscosifier-mixing case. While data show discrepancies in the evolution of d_F

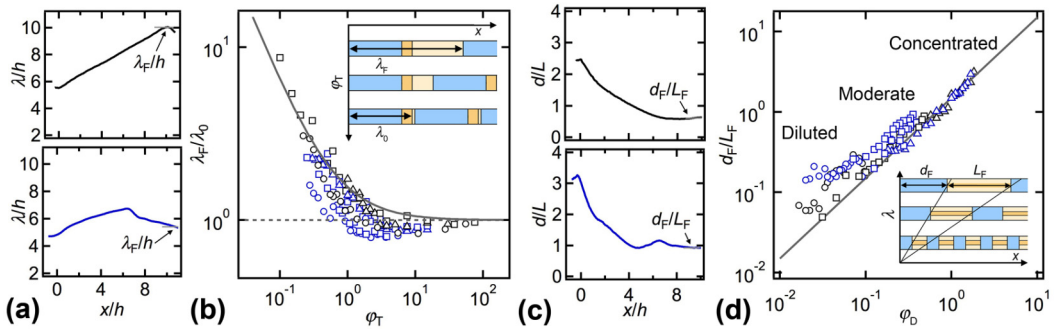

FIG. 4. Deformation of segmented flows. (a) Spatial evolution of wavelength λ for cases shown in Figs. 3(d) (top) and 3(e) (bottom). (b) Evolution of normalized final wavelength λ_F/λ_0 as function of thread flow rate ratio $\varphi_T = (Q_1 + Q_2)/Q_3$ for various $\alpha_1 = 0.09(\bigcirc)$, 0.33 ($\square$), 0.67 ($\triangle$), and fluid groups $M3$ (blue) and $D2$ (black). Solid line: $\lambda_F/\lambda_0 = 1 + 1/(k_o\varphi_T)$, with $k_0 = 1.8$. Inset: schematic of linear dilution model. (d) Spatial development of aspect ratio d/L for cases shown in Figs. 3(d) (top) and 3(e) (bottom). (d) Final aspect ratio d_F/L_F as a function of droplet flow rate ratio $\varphi_D = Q_1/(Q_2 + Q_3)$. Solid line: $d_F/L_F = a\varphi_D$, with $a = 1.5$. Inset: schematics of segmented flows having fixed d_F/L_F and various λ_F.

based on fluid group $D3$ or $M2$ in the viscosifier-mixing region, the spacing between droplets L_F appears to remain independent of the fluid group. The spatial evolutions of d and L are displayed in Figs. 3(d) and 3(e) where fluid flow rates are identical for both fluid groups for $\alpha_1 = 0.67$ and $\alpha_F = 0.75$. In both cases, the droplet experiences a recoil in the streamwise direction at the junction and an extension as it fully enters the observation channel downstream. For large viscosity contrasts with fluid group $D3$, the droplet then continuously decreases in size as the capillary number declines due to mixing and rearrangement of phases. For moderate χ with fluid group $M2$, mixing and rearrangement eventually produce a large Ca and the droplet is seen to further increase in δ as the thin film becomes non-negligible. Observations of these flows at the droplet level clearly evidence micromixing in the continuous phase.

The droplet size d and spacing L experience complex variations in the observation channel; therefore the overall morphological evolution of segmented flows is examined based on final wavelength $\lambda_F = d_F + L_F$ and aspect ratio d_F/L_F. The wavelength λ is expected to grow in the observation channel as a result of droplet dilution due to the added fluid $L3$. Different behaviors are observed due to droplet variation in size d and mobility coefficient k [Fig. 4(a)]. For simple dilution processes, the final λ_F is assumed to follow $\lambda_F = \lambda_0 + Q_3T_0/h^2$, where T_0 is the period of the initial segmented flow, which corresponds to the time necessary for a new unit cell to enter the second section. As $T_0 = \lambda_0/V_0$ and $V_0 = k_0(Q_1 + Q_2)/h^2$, the relative wavelength is modeled as $\lambda_F/\lambda_0 = 1 + 1/(k_o\varphi_T)$. As can be seen in Fig. 4(b), significant departure from this behavior is observed when φ_T is near unity in the tubing regime. For larger thread flow rate ratio φ_T, the new λ_F is smaller than the initial λ_0 since droplet mobility k decreases due to a sharp change in Ca and, as a result, segmented flows become more compact. For very small $\varphi_T \ll 1$ in the threading regime, good agreement is found between measurement and prediction. Although flows may not be fully developed at the end of the observation channel, these data suggest that the wavelength of segmented flow λ strongly depends on the droplet mobility coefficient k, which provides a measure of the effective drift between each phase. By contrast, the aspect ratio d/L is a representation of mass conservation within a stable unit cell. While d and L vary along the flow direction, the ratio d/L quickly stabilizes [Fig. 4(c)]. Besides the evolving continuous phase, the overall final aspect ratio scales linearly with the flow rate ratio based on droplets, $\varphi_D = Q_1/(Q_2 + Q_3)$, according to $d_F/L_F = a\varphi_D$, where the coefficient $a = 1.5$ is similar to the one observed for the initial segmented flow $d_0/L_0 = 1.5\,\varphi_1$ [Fig. 1(d)]. As viscous stratifications modify droplet dynamics, reciprocally droplets create significant agitation of stratifications.

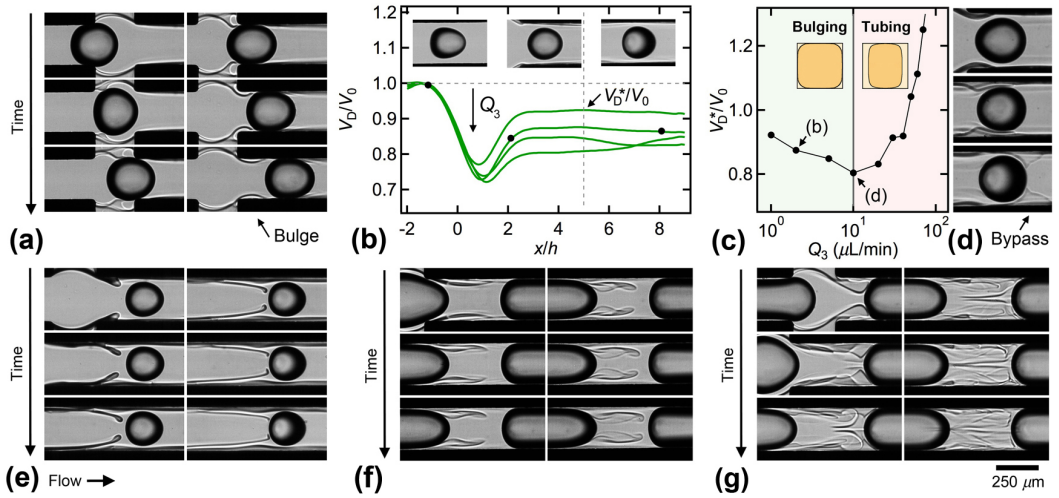

FIG. 5. Bulging regime. Flow rates in μl/min. (a) Time series of droplet entering the second junction and pulling low-viscosity bulges for [$(Q_1, Q_2, Q_3) = (1, 10, 1)$, group $M2$] and $\Delta t = 30$ ms. (b) Spatial evolution of V_D/V_0 at low α_1 and large Ca_0, symbols correspond to top micrographs for [(5, 50, 2), $M2$] (c) Evolution of V_D^*/V_0 with Q_3 for group $M2$ at low α_1 and large Ca_0. (d) Spatial evolution of droplet showing bulges bypass at the tubing transition, $x/h \approx 2$, 5, and 8 (from top to bottom). (e) Time series of ligament entrainment in droplet reference frame for [(5, 50, 2), $D3$] and $\Delta t = 10$ ms. (f) Time series of viscous sheet formation in droplet reference frame for [(20, 10, 1), $M2$] and $\Delta t = 20$ ms. (g) Flowering pattern of recirculating threads in droplet reference frame for [(20, 10, 4), $D3$] and $\Delta t = 20$ ms.

V. THREAD FLOW REGIMES

Viscous thread-forming flows are strongly destabilized by the passage of microfluidic droplets. Since lubricating transitions of the central stream are controlled by φ_T, each thread regime, such as bulging, tubing, and threading, is discussed based on initial droplet concentration α_1 and size d_0. On the one hand, low droplet concentrations $\alpha_1 = 0.09$ are associated with small droplet sizes $d_0/h \approx 0.97$ and initially diluted flows permit investigating the role of small individual droplets on threads in the viscosifier regime at small φ_T. On the other hand, concentrated flows at large $\alpha_1 = 0.67$ are made of long droplets $d_0/h \approx 3.86$ separated by short distance $L_0/h \approx 1.29$, which produces complex recirculating flows of low- and high-viscosity fluids and enhances mixing in the thinner regime at large φ_T. This microfluidic system offers a rare window into the formation of regular, yet intricate miscible flow structures at low Re due to individual and collective influence of droplets.

A. Bulging

The bulging regime corresponds to large thread flow rate ratios $\varphi_T \gg 1$. In the absence of droplets, this flow pattern consists of a pipe flow of the more viscous oil $L2$ in contact with the four walls of the square microchannels and the low-viscosity, more mobile fluid $L3$ percolating the pile through the four corners of the square channel. Given that $Q_1 + Q_2 \gg Q_3$, the central stream also extends in the side channels of the second junction, producing high-viscosity bulges. In hydrodynamic focusing sections, this regime is typically labeled as "displacement" for the case of immiscible fluids. Here, the presence of droplet brings information about the structure and dynamics of the central pile. In particular, the displacement of droplets through the second junction entrains the low-viscosity fluids $L3$ in the form of small bulges in the trail of the droplets [Fig. 5(a)]. As thin fluid is deposited at the walls, low-viscosity bulges adopt various dynamics. In particular, protuberances

of low-viscosity fluid are seen to slowly travel near the channel edges with a celerity c that remains lower than the droplet velocity V_D.

When a droplet passes through the junction, the thin fluid $L3$ rapidly covers the droplet interfacial area, which lowers the local capillary number Ca in the vicinity of the droplet. The depression of Ca induces a reduction of the thin lubricating film δ between droplets and walls, and droplets laterally swell to become more compact. An example of droplet rearrangement from a bullet shape to a sphere along the flow path is displayed in Fig. 5(b), inset. As the diminution of δ is also accompanied with a reduction of droplet "lubricating effects," which typically facilitate motion, the velocity V_D in the outlet channel becomes lower than the inlet droplet velocity V_0 despite the presence of fluid $L3$ that is added at a volumetric rate of Q_3 [Fig. 5(b)]. The characteristic velocity V_D^* is measured at $x/h = 5$ and is found to decrease with Q_3 until the transition to the tubing regime [Fig. 5(c)]. At this point, the droplet velocity V_D^* reaches a minimum value and trailing bulges bypass the droplet as the high-viscosity pile $L2$ progressively detaches from the side walls [Fig. 5(d)].

The bulging regime displays rich dynamics, such as the entrainment of bulges in the form of ligaments in the bulk of $L2$. Such ligaments produce low-viscosity striations of the pile and progressively thin to form low-viscosity currents [Fig. 5(e)]. In the concentrated droplet regime at $\alpha_1 = 0.67$, bulges are distorted due to the close proximity and interaction between droplets. As long droplets act as leaky pistons that compartment the continuous phase, bulges can evolve into "viscous sheets" [Fig. 5(f)]. Finally, near the tubing transition, complex interactions between thread partial lubrication and droplet lower mobility produce an intriguing regime labeled as "flowering" by visual analogy [Fig. 5(g)]. In this case, the pile appears to split into multiple threads entrained in recirculating flow patterns. This regime offers attractive features for in-line micromixing applications of high- and low-viscosity fluids in the situation where a thinner is added to a thick material.

B. Tubing

The tubing regime is established when the central stream of $L2$ is partially lubricated with the thin fluid $L3$ near the side walls. The transition from bulging to tubing is apparent with the presence of trailing bulges bypassing droplets made of $L1$. For the diffusive fluid group $M3$, a viscous fingering instability is observed for low velocities Fig. 6(a). Viscous digitation or Saffman-Taylor instabilities are typically observed when a low-viscosity fluid displaces a more viscous liquid and forms fingers in confined environments [26–29]. Here, as droplets enter stratifications, the central viscous layer progressively replenishes near the droplet trail, which displaces the excess $L3$ fluid past the droplets near the channel wedges. While for large Péclet number Pe, the excess fluid forced through the channel corners continues to travel in a form of protuberances along the central stream at a celerity $c > V_D$, for low Pe, the growth of distinguishable fingers of width f indicates diffusive mixing processes where fluids of various reflective index blend. The evolution of f is measured at various φ_T through spatiotemporal analysis of high-speed imaging and show in Fig. 6(b) as a function of $t - t_0$, where t_0 corresponds to the instant when fingers become optically discernable. The growth of f is initially linear in time with a nearly constant diffusive velocity $J_{\mathrm{Diff}} = df/dt \approx 2.4\,\mathrm{mm/s}$, which yields a critical $\mathrm{Pe} = hJ_{\mathrm{Diff}}/D$ of 107 for the diffusion-convection transition. For mature viscous digitations $f/h > 1$, fingers can centrally merge [Fig. 6(c)] or deform due to convective processes in the tubing regime [Fig. 6(d)], which result in effective variations of J_{Diff} at later times. This phenomenon is characteristic of the diluted droplet regime at low speed with diffusive fluids.

Dynamics of the tubing regime consists of a large velocity difference between side streams and the central pile similar to the plane geometry configuration [30,31]. Here, as the thread flow rate ratio φ_T decreases, the droplet velocity progressively rises, as shown for the case of the small diluted droplet regime in Fig. 6(e). Complex rearrangements of the central layer at the back of droplets produces spatial evolution of the droplet speed. As φ_T further declines, a persistent lubricated thread is seen behind the droplet while the flow remains in the partially lubricated tubing regime ahead of the droplet. When a stable thread is finally formed on both side of the droplets for $\varphi_T < 0.4$, the

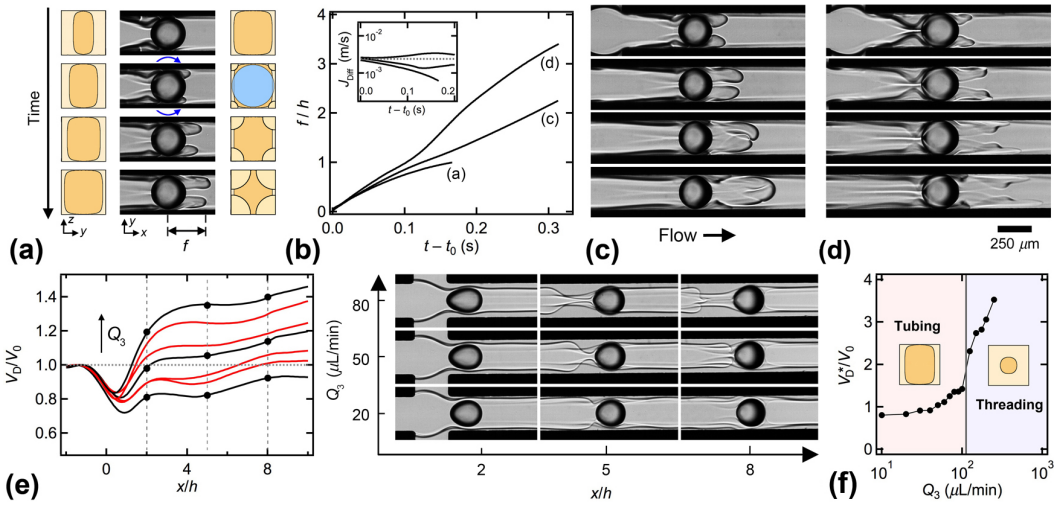

FIG. 6. Tubing regime. Flow rates in μl/min (a) Time-series of viscous fingering in the droplet reference frame, [$(Q_1, Q_2, Q_3) = (1, 10, 2)$, group $D3$], and $\Delta t = 40$ ms. Side schematics show upstream and downstream cross-sections. (b) Evolution of finger width f as a function of time $t - t_0$. Inset: J_{Diff} vs. time, dashed-line: $J_{\mathrm{Diff}} = 2.4$ mm/s. (c) Time-series of merging diffusive fingers in the droplet reference frame, [(1,10,3), $D3$], and $\Delta t = 65$ ms. (d) Time-series showing convective distortion of fingers in the droplet reference frame [(1,10,4), $D3$], and $\Delta t = 60$ ms. (e) Spatial evolution of V_{D}/V_0 for low α_1 and large Ca_0. Symbols correspond to micrographs for [$(Q_1, Q_2) = (5, 50)$, group $M2$]. (g) Evolution of V_D^* with Q_3 from tubing to threading regime for [(5,50), $M2$].

characteristic droplet speed V_D^* gains significant magnitude at the tubing-threading regime transition [Fig. 6(f)].

C. Threading

The threading regime corresponds to a fully lubricated thread convected at V_{T} near the peak velocity of the parabolic sheath flow. As droplet velocity V_D, however, typically scales with average flow velocity, notable velocity differences arise between threads and droplets. In particular, a thread thinning behavior is observed near slow-moving droplets. Similar to previous regimes, the droplet speed displays a nontrivial behavior due to viscous multilayer rearrangements. While V_D initially increases as droplets are injected into the fast-moving fluid, the velocity reaches a peak value V_D^* around $x/h = 5$ before progressively decreasing downstream [Fig. 7(a)]. As $V_{\mathrm{T}} > V_{\mathrm{D}}$, both front and rear thread thicknesses ε_{F} and ε_{R} decrease at different rates since high-viscosity fluid $L2$ is transferred from the back to the front of the droplet. The thread thinning behavior around a droplet along the flow direction is evident in the micrographs in Fig. 7(a). When the rear thread is thin enough, a viscous folding instability is observed in the second part of the observation channel. Evidence of $L2$ fluid bypass is evident though the partial coating of larger droplets at large $\chi \sim 10^3$ [Fig. 7(b)].

To better understand the thread thinning processes, the initial thread size ε_0 is measured before droplets enter the strata and show good agreement with the expected scaling $\varepsilon_0/h \sim \varphi_{\mathrm{T}}^{1/2}$ [Fig. 7(c)]. The initial thread width ε_0 provides a length scale to examine the spatial evolution of ε_{F} and ε_{R} at various flow rates. Image analysis of high-speed movies is conducted at low α_1 to measure ε_{R} at a distance $x = x_B - h$, where x_B is the position of the back of a droplet, and ε_{F} at $x = x_{\mathrm{F}} + h$, where x_{F} is the position of the front of a droplet. The spatial development of normalized widths collapses onto distinct curves for ε_{F} and ε_{R} at different φ_T [Fig. 7(d)]. While the front thread size ε_{F} displays a

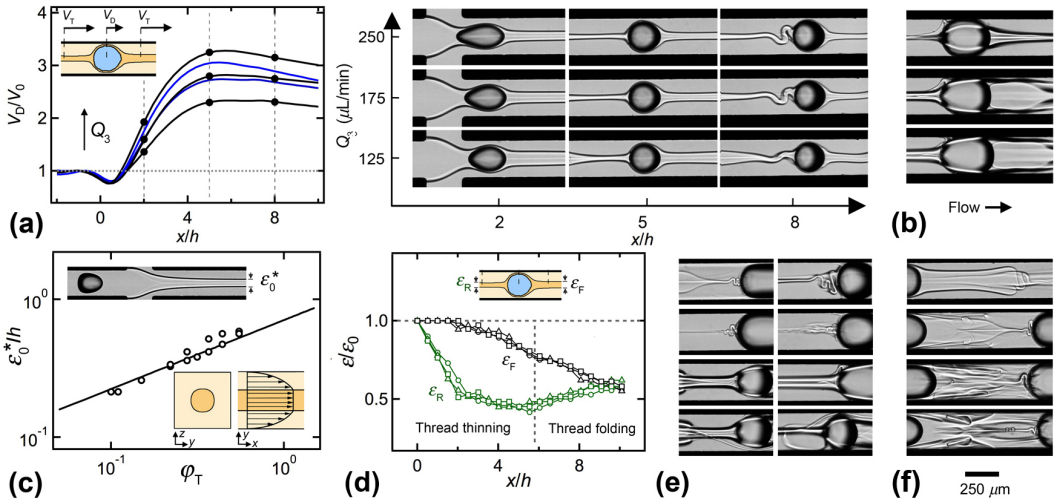

FIG. 7. Threading regime. Flow rates in μl/min. (a) Spatial evolution of V_D/V_0 for low α_1 and large Ca_0, group $M2$. Symbols correspond to micrographs where $(Q_1, Q_2) = (5, 50)$. Inset: schematics of droplet and thread velocities. (d) Examples of droplet partial envelopment with $L2$ for $(Q_1, Q_2) = (5, 10)$, and $Q_3 = 300$, 200, and 125 (from top to bottom) with group $D3$. (c) Normalized thread size ε_0^*/h as a function of φ_T, solid line: $\varepsilon_0/h = (\varphi_T/2)^{1/2}$. Top inset: example of micrograph used to measure ε_0^*. Bottom insets: schematics with plug velocity profile. (d) Spatial evolution of $\varepsilon_F/\varepsilon_0$ and $\varepsilon_R/\varepsilon_0$ for low α_1 and large Ca_0 with (Q_1, Q_2)=(5, 50) and $Q_3 = 125$(◯), 175 (□), 200 (△) with group $M2$. Inset: schematic of measurements. (e) Thread buckling modes. From left to right: folding [$(Q_1, Q_2, Q_3) = (20, 10, 25)$, group $M2$], subfolding [(25, 50, 175), $M2$]; thread thinning [(20, 10, 125), $M2$]; dissolving thread [(1, 10, 150), $M2$], internal folding [(5, 50, 200), $D3$], folding collapse [(5, 10, 125), $D3$], and alternating shooting threads, bottom thread (left) followed by top thread (right) [(1, 10, 50), $D3$]. (f) Pile buckling. From top to bottom: structural buckling [(25, 50, 150), $M2$], edge buckling [(20, 10, 14), $M2$], diffusion-induced buckling [(20, 10, 15), $D3$] and [(20,10,25), $D3$].

nearly linear decrease along the flow direction, data show a nonmonotonic behavior for the rear size ε_R with a sharp initial decrease to about half of ε_0 between $x/h \approx 0$ and 2, followed by a plateau between $x/h \approx 2$ and 6, and a slow growth in the folding region for $x/h > 6$ A main feature of segmented flows of thread is the spatial transition to viscous buckling instabilities at a fixed distance from the junction. The emergence of viscous thread folding allows for excess high-viscosity fluid storage in the back of the droplet and a reduction of $L2$ bypassing of droplets.

Over the range of parameters investigated, several viscous buckling modes are identified, including folding, subfolding, subfolding with thinning, and diffusive folding. Other modes include folding within thread and "shooting threads" [Fig. 7(e)]. The pile can also buckle, either in its structure or through the edges. In case of strong diffusion, highly complex flow with multiple threads is observed [Fig. 7(f)]. The destabilization of lubricated threads through folding instabilities increases miscible interfacial areas between low- and high-viscosity fluids and improves blending of fluids in the viscosifier-mixing regime.

VI. CONCLUSIONS

In this work, an experimental approach is employed to reveal the influence of the outer fluid viscosity on the microflow of droplets and examine the destabilization of miscible fluid threads with droplets. Initial droplet flows are set at various α_0 to fix droplet size d_0 and spacing L_0 and thread-forming flows are manipulated with φ_T to modify thread size ε_0. Diffusive and weakly diffusive miscible fluid groups of different viscosity ratios χ are investigated to document the influence of Péclet and capillary numbers on microfluidic multiphase arrangements of viscous fluids.

The first part focuses on the modification of segmented flows and examines breakup and nonbreakup droplet regimes. The spatial evolution of droplet velocity V_D is strongly correlated with thread flow regimes defined by the state of lubrication of the central stream. Mixing in the continuous phase contributes to lowering the capillary number in the observation channel resulting in nonmonotonic variations of droplet size d. Segmented flows are compared with the expected wavelength λ and aspect ratio d/L of regularly alternated fluid sequences during microfluidic dilution. While the aspect ratio of droplet patterns is well predicted, the wavelength of the unit cell significantly deviates from modeling for droplets implanted in partially lubricated threads in the tubing regime.

In the second part, viscous thread formation is examined at various φ_T to quantify the influence of droplet size d_0. In the bulging regime, at large φ_T, the central stream "wets" the four walls and droplet velocity decreases due to reduction of Ca and phase rearrangements. Low-viscosity bulges are entrained in the viscous pile providing a mechanism to enhance blending for thinner-mixing applications. In the tubing regime, at moderate φ_T, a viscous fingering instability is reported between droplets and thread-forming flows at low Pe. In the threading regime, for low φ_T, the central stream thins at different rates around droplets, leading to a variety of viscous buckling instabilities, which enlarge the interfacial area and reduce the fluid diffusional path to improve blending for viscosifier-mixing applications.

This works clarifies regions in the parameter space where low- and high-viscosity fluid mixing is enhanced due to the presence of droplets. It is shown in particular that microfluidic technology is useful for adding a thinner to a viscous fluid near the transition between bulging and tubing regimes at large droplet concentrations. The other configuration where a viscosifier is added to a thin fluid corresponds to the threading regime where droplets of low mobility provide impinging surfaces for buckling threads. Microfluidic platforms provide an advanced fluid dynamics laboratory to examine the role of fluid properties on basic phenomena, which can be combined into various sequences and geometrical arrangements to reveal flow regimes of practical interest.

ACKNOWLEDGMENT

This material is based upon work supported by the National Science Foundation under Grant No. CBET-1150389.

[1] G. K. Batchelor, *An Introduction to Fluid Mechanics* (Cambridge University Press, New York, 1967).
[2] D. D. Joseph and Y. Y. Renardy, Fundamentals of two-fluid dynamics, *Part II: Lubricated Transport, Drops and Miscible Liquids* (Springer-Verlag, New York, 1993).
[3] A. Z. Zinchenko and R. H. Davis, Motion of deformable drops through porous media, Annu. Rev. Fluid Mech. **49**, 71 (2017).
[4] C. N. Baroud, F. Gallaire, and R. Dangla, Dynamics of microfluidic droplets, Lab Chip **10**, 2032 (2010).
[5] R. Seemann, M. Brinkmann, T. Pfohl, and S. Herminghaus, Droplet based microfluidics, Rep. Prog. Phys. **75**, 016601 (2011).
[6] S. L. Anna, Droplets and bubbles in microfluidic devices, Annu. Rev. Fluid Mech. **48**, 285 (2016).
[7] R. K. Shah, H. C. Shum, A. C. Rowat, D. Lee, J. J. Agresti, A. S. Utada, L.-Y. Chu, J.-W. Kim, A. Fernandez-Nieves, C. J. Martinez *et al.*, Designer emulsions using microfluidics, Mater. Today **11**, 18 (2008).
[8] J. D. Tice, A. D. Lyon, and R. F. Ismagilov, Effect of viscosity on droplet formation and mixing in microfluidic channels, Anal. Chim. Acta **507**, 73 (2004).
[9] A. Günther, M. Jhunjhunwala, M. Thalmann, M. A. Schimdt, and K. F. Jensen, Micromixing of miscible liquids in segmented gas-liquid flow, Langmuir **21**, 1547 (2005).

[10] T. Cubaud, B. M. Jose, S. Darvishi, and R. Sun, Droplet breakup and viscosity-stratified flows in microchannels, Int. J. Multiphase Flow **39**, 29 (2012).
[11] X. Chen and C. L. Ren, Experimental study on droplet generation in flow focusing devices considering a stratified flow with viscosity contrast, Chem. Eng. Sci. **163**, 1 (2017).
[12] T. J. Ober, D. Foresti, and J. A. Lewis, Active mixing of complex fluids at the microscale, Proc. Natl. Acad. Sci. USA **112**, 12293 (2015).
[13] H. M. Xia, Z. P. Wang, Y. X. Koh, and K. T. May, A microfluidic mixer with self-excited 'turbulent' fluid motion for wide viscosity ratio applications, Lab Chip **10**, 1712 (2010).
[14] S. L. Perry, J. J. L. Higdon, and P. J. A. Kenis, Design rules for pumping and metering of highly viscous fluids in microfluidics, Lab Chip **10**, 3112 (2010).
[15] S. Wang, X. Huang, and C. Yang, Mixing enhancement for high viscous fluids in a microfluidic chamber, Lab Chip **11**, 2081 (2011).
[16] S. Orbay, A. Ozcelik, J. Lata, M. Kaynak, M. Wu, and T. J. Huang, Mixing high-viscosity fluids via acoustically driven bubbles, J. Micromech. Microeng. **27**, 015008 (2017).
[17] T. Cubaud and T. G. Mason, Interacting viscous instabilities in microfluidic systems, Soft Matter **8**, 10573 (2012).
[18] T. Cubaud and S. Notaro, Regimes of miscible fluid thread formation in microfluidic focusing sections, Phys. Fluids **26**, 122005 (2014).
[19] S. Tottori and S. Takeuchi, Formation of liquid rope coils in a coaxial microfluidic device, RSC Adv. **5**, 33691 (2015).
[20] B. Xu, J. Chergui, S. Shin, and D. Juric, Three-dimensional simulations of viscous folding in diverging microchannels, Microfluid. Nanofluid. **20**, 140 (2016).
[21] T. Cubaud, D. Henderson, and X. Hu, Separation of highly viscous fluid threads in branching microchannels, Microfluid. Nanofluid. **20**, 55 (2016).
[22] S. Gosh, G. Das, K. Prasanta, and K. Das, Liquid buckling in a practical situation, Eur. Phys. Lett. **115**, 44004 (2016).
[23] S. Jakiela, S. Makulska, P. M. Korczyk, and P. Garstecki, Speed of flow of individual droplets in microfluidic channels as a function of the capillary number, volume of droplets and contrast of viscosities, Lab Chip **11**, 3603 (2011).
[24] B. M. Jose and T. Cubaud, Formation and dynamics of partially wetting droplets in square microchannels, RSC Adv. **4**, 14962 (2014).
[25] T. Cubaud, M. Tatineni, X. Zhong, and C.-M. Ho, Bubble dispenser in microfluidic devices, Phys. Rev. E **72**, 037302 (2005).
[26] G. M. Homsy, Viscous fingering in porous media, Annu. Rev. Fluid Mech. **19**, 271 (1987).
[27] E. Lajeunesse, J. Martin, N. Rakotomalala, D. Salin, and Y. C. Yortsos, Miscible displacement in a Hele-Shaw cell at high rates, J. Fluid Mech. **398**, 299 (1999).
[28] T. Suekane, J. Ono, A. Hyodo, and Y. Nagatsu, Three-dimensional viscous fingering of miscible fluids in porous media, Phys. Rev. Fluids **2**, 103902 (2017).
[29] T. Soori and T. Ward, Stable and unstable miscible displacement of a shear-thinning fluid at low Reynolds number, Phys. Fluids **30**, 103101 (2018).
[30] T. Cubaud and T. G. Mason, Formation of miscible fluid microstructures by hydrodynamic focusing in plane geometries, Phys. Rev. E **78**, 056308 (2008).
[31] M. E. Kurdzinski, B. Gol, A. C. Hee, P. Thurgood, J. Y. Zhu, P. Petersen, A. Mitchell, and K. Khoshmanesh, Dynamics of high viscosity contrast confluent microfluidic flows, Sci. Rep. **7**, 5945 (2017).